



Cite this: DOI: 10.1039/d1sm00019e

## Plateau–Rayleigh instability in a soft viscoelastic material

S. I. Tamim and J. B. Bostwick \*

A soft cylindrical interface endowed with surface tension can be unstable to wavy undulations. This is known as the Plateau–Rayleigh instability (PRI) and for solids the instability is governed by the competition between elasticity and capillarity. A dynamic stability analysis is performed for the cases of a soft (i) cylinder and (ii) cylindrical cavity assuming the material is viscoelastic with power-law rheology. The governing equations are made time-independent through the Laplace transform from which a solution is constructed using displacement potentials. The dispersion relationships are then derived, which depend upon the dimensionless elastocapillary number, solid Deborah number, and compressibility number, and the static stability limit, critical disturbance, and maximum growth rate are computed. This dynamic analysis recovers previous literature results in the appropriate limits. Elasticity stabilizes and compressibility destabilizes the PRI. For an incompressible material, viscoelasticity does not affect stability but does decrease the growth rate and shift the critical wavenumber to lower values. The critical wavenumber shows a more complex dependence upon compressibility for the cylinder but exhibits a predictable trend for the cylindrical cavity.

Received 6th January 2021,  
Accepted 13th March 2021

DOI: 10.1039/d1sm00019e

[rsc.li/soft-matter-journal](http://rsc.li/soft-matter-journal)

## 1 Introduction

Surface tension arises from molecular interactions at the interface between two immiscible materials. For liquids, surface tension forces dominate the response, *i.e.* flow, when the length scale of the system  $L$  is smaller than the capillary length  $\ell_c = \sqrt{\sigma/\rho g}$ ,  $L < \ell_c$ , where  $\sigma$  is the surface tension,  $\rho$  the density and  $g$  the gravitational constant. The literature for these capillary flows is vast and well-studied in the fluid mechanics community. Solids also possess a surface tension,<sup>1,2</sup> but this is often neglected as elasticity typically dominates the response for most common materials, *e.g.* metals or ceramics. Surface tension becomes important in solids when  $L$  is smaller than the elastocapillary length  $\ell_e \equiv \sigma/E$ ,  $L < \ell_e$ , where  $E$  is the elastic modulus, and studies of such systems belong to the field of elastocapillarity.<sup>3,4</sup> Many soft gels have  $E \sim 10$  Pa, such that  $\ell_e \sim 1$  mm, and it is therefore unsurprising that many classical capillary instabilities have been observed in soft solids, such as the buoyancy-driven Rayleigh–Taylor instability,<sup>5,60</sup> the Saffman–Taylor instability,<sup>7</sup> parametrically-excited Faraday waves,<sup>8</sup> and drop oscillations.<sup>6,9</sup> In this paper, we analyze the Plateau–Rayleigh instability of a soft viscoelastic cylinder.

A liquid cylinder will breakup into droplets due to surface tension, as is commonly seen in a dripping faucet. Plateau<sup>10</sup> used a static energy analysis to show that a cylinder with length longer than its circumference is unstable. This is the Plateau

limit. This static analysis, however, is unable to predict the final drop size and associated wavelength of the instability. It was Rayleigh,<sup>11,12</sup> who used a dynamic stability analysis to give a dispersion relationship that was able to determine the wavenumber with fastest growth rate and correctly predict the final drop size. For this reason, this has come to be known as the Plateau–Rayleigh instability, hereafter simply referred to as PRI.

Mora *et al.*<sup>13</sup> have observed PRI in soft agar gels using a novel experimental approach in which gel cylinders are cast in polystyrene molds are then immersed in toluene, which dissolves the mold and allows the instability to develop. Here they observe permanent undulations of the cylinder, but not complete breakup into drops, when  $\ell_e/R > 6.2$ . They perform a static stability analysis for a linear elastic cylinder to correctly predict this limit. Note that this is similar to the approach of Plateau. We use a dynamic analysis to predict the dispersion relationship from which the critical wavenumber of maximum growth rate is obtained, as it depends upon elastocapillarity, viscoelasticity, and compressibility. In this sense, our work is complementary to that of Mora *et al.*<sup>13</sup> in the same way that Rayleigh's dynamic analysis complemented the static analysis of Plateau.

PRI in soft solids is of interest to 3D bioprinting technologies<sup>14,62</sup> and nonstandard inkjet,<sup>15</sup> patterning of microfluidic devices,<sup>16,17</sup> and pathologies related to biological tubes.<sup>18,19</sup> PRI in solids is different from fluids in that the competition between elastic and capillary energy can give rise to stable corrugated patterns.<sup>20–23</sup> This can be viewed as a phase separation between different regions of stretch that forms the beads-on-a-string structure due to PRI.<sup>24–26</sup> The

Department of Mechanical Engineering, Clemson University, Clemson, SC 29634, USA. E-mail: [jbostwi@clemson.edu](mailto:jbostwi@clemson.edu)

cylindrical cavity is the complementary problem to the cylinder and has also received some attention recently.<sup>27–29</sup> We analyze both the cylinder and cylindrical cavity in this work.

Soft materials often exhibit a complex rheology and are characterized as viscoelastic materials with both an elasticity and viscosity, which are often frequency dependent.<sup>30,31</sup> Gels are one class of soft material that typically consists of a cross-linked polymer network that generally behaves as a solid with tunable elasticity.<sup>32</sup> The crosslinking networks present in these materials exhibit stress relaxation behaviour over a finite timescale which is typical of viscoelastic solids.<sup>33</sup> This viscoelastic relaxation of hydrogels can be manipulated to mimic behaviour of muscle tissues.<sup>34</sup> During 3D bioprinting, viscoelasticity of bioinks are known to affect the printability and structural integrity.<sup>35</sup> They are also used in creating biopolymers for numerous medical applications.<sup>36</sup> Polyacrylamide microgels are used to 3D print extracellular matrices,<sup>37</sup> while PDMS have recently seen its use in 3D printing active structure that responds to external stimuli.<sup>38</sup> Commonly used soft hydrogels like agarose behave essentially as a linear elastic material for small strains<sup>39</sup> and has a capillary effect that is comparable to the bulk elasticity.<sup>9</sup> Materials with a more complex rheology can exhibit more complex behaviors that lead to experimentally-observed stick-slip motions during the spreading of a liquid over a soft material.<sup>40,41</sup> Here viscous, elastic, and capillary forces are all of similar magnitude.<sup>42</sup> Notably, Karpitschka *et al.*<sup>43</sup> have developed a model for a moving contact-line over a viscoelastic substrate recovering these stick-slip motions. These models are based on viscoelastic solids like PDMS that follow a power-law rheology with the characteristic viscoelastic timescale being in the range of 0–1 s. In our model development, we take a similar approach and assume the soft viscoelastic material behaves as a power-law gel which admits a characteristic time scale that becomes zero in the purely elastic limit.<sup>44,45</sup> Viscoelastic fluids are also characterized with a slow relaxation timescale which increases with elasticity.<sup>46</sup> In this work we choose the capillary timescale in line with recent viscoelastic modelling approaches,<sup>47</sup> which allows us to compare our results to classical results of PRI.

We begin this paper by defining the governing equations for a soft viscoelastic (i) cylinder and (ii) cylindrical cavity in Section 2. A solution is constructed in Section 3 by introducing displacement potentials, which gives rise to a dispersion relationship that depends upon dimensionless numbers that define elastocapillary, viscoelastic, and compressibility effects. In Section 4, we show how the dispersion relationship and stability characteristics are affected by the dimensionless numbers and we note that we recover previous results in the appropriate limit. Lastly, we end with some concluding remarks and discuss future directions.

## 2 Formulation

Consider a cylindrical rod of radius  $R$  in a cylindrical coordinate system  $(r, \theta, z)$ , as shown in Fig. 1(a). This soft material is characterized by a density  $\rho$ , Lamé parameters  $\lambda, \mu$ , Poisson ratio  $\nu$ , and the interface is endowed with a surface tension  $\sigma$ . Our analysis presented herein is sufficiently general such that it is

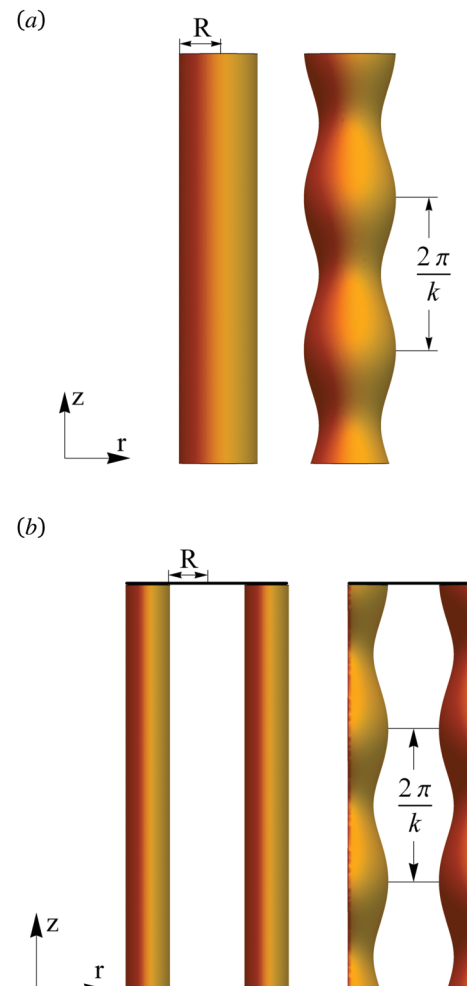


Fig. 1 Definition sketches for the soft (a) cylinder and (b) cylindrical cavity.

straightforward to also consider the complementary case of the cylindrical cavity in a soft material, as shown in Fig. 1(b). In what follows, we perform a parallel analysis of these two problems.

### 2.1 Field equations

The soft solid is assumed to be a linear viscoelastic material with the stress field  $\tau_{ij}$  and strain field  $\varepsilon_{ij}$  related by,<sup>48</sup>

$$\tau_{ij}(t) = 2 \int_{-\infty}^t \mu(t-t') \frac{\partial \varepsilon_{ij}(t')}{\partial t'} dt' + \delta_{ij} \int_{-\infty}^t \lambda(t-t') \frac{\partial \varepsilon_{kk}(t')}{\partial t'} dt', \quad (1)$$

where  $\mu(t)$  and  $\lambda(t)$  are the relaxation moduli, which are related to one another through the Poisson ratio  $\nu$ ,  $\lambda = 2\nu/(1-2\nu)\mu$ . The strain field  $\varepsilon_{ij}$  is related to the displacement field  $\mathbf{U}$ ,

$$\varepsilon_{ij} = \frac{1}{2} \left( \frac{\partial U_i}{\partial x_j} + \frac{\partial U_j}{\partial x_i} \right). \quad (2)$$

The equation of motion is given by Newton's second law

$$\frac{\partial \tau_{ij}}{\partial x_j} = \rho \frac{\partial^2 U_i}{\partial t^2}. \quad (3)$$

The jump in normal stress across the free surface boundary  $r = R$  is given by the Young–Laplace equation and is proportional to the linearized curvature,

$$\tau_{rr}^e - \tau_{rr}^i = -\sigma \left( \frac{\partial^2 u_r}{\partial z^2} + \frac{u_r}{R^2} \right), \quad (4)$$

valid for small disturbances  $u_r \ll 1$ . Here  $i, e$  denote the inner and exterior material, respectively. For the cylinder  $\tau^e = 0$ , whereas for the cylindrical cavity  $\tau^i = 0$ . Continuity of shear stress is also enforced,

$$\tau_{rz} = \tau_{r\theta} = \tau_{z\theta} = 0. \quad (5)$$

## 2.2 Normal modes

Normal modes  $e^{st}$  are assumed with  $s$  is the growth rate, *e.g.* the displacement field is defined as  $\mathbf{U} = \mathbf{u}(r, \theta, z)$  with  $\mathbf{u}(r, \theta, z) = u_r(r, \theta, z)\hat{e}_r + u_\theta(r, \theta, z)\hat{e}_\theta + u_z(r, \theta, z)\hat{e}_z$  the time-independent field. We choose to work with the growth rate  $s$  instead of the frequency  $\omega$  because our focus is on instability  $s > 0$ . We take the following Laplace transform,

$$f(s) = \int_0^\infty f(t)e^{-st}dt \quad (6)$$

and apply it to the constitutive relationship (1) to get,

$$\tilde{\tau}_{ij}(s) = 2\tilde{\mu}(s)\tilde{e}_{ij}(s) + \delta_{ij}\tilde{\lambda}(s)\tilde{e}_{kk}(s), \quad (7)$$

where the complex shear modulus  $\tilde{\mu}(s)$  is defined as,

$$\tilde{\mu}(s) = \tilde{\mu}'(s) + i\tilde{\mu}''(s) = s \int_0^\infty \Psi(t)e^{-st}dt. \quad (8)$$

Here  $\tilde{\mu}'(s)$  and  $\tilde{\mu}''(s)$  are the storage and loss modulus, respectively, and  $\Psi$  is the relaxation function which is determined by the rheology of the material. For a complex solid, they are both a function of the frequency, or in our particular case, unstable growth rate. In most cases, the Poisson ratio  $\nu$  is considered to be constant and independent of the frequency and therefore  $\lambda = 2\mu\nu/1 - 2\nu$ . Using (7) and the normal mode solution, the governing eqn (3) can be written as

$$(\tilde{\lambda}(s) + \tilde{\mu}(s))\nabla(\nabla \cdot \mathbf{u}) + \tilde{\mu}(s)\nabla^2 \mathbf{u} = \rho s^2 \mathbf{u}. \quad (9)$$

The boundary conditions (4) and (5) have no explicit time dependence and follow similarly.

## 2.3 Rheology of soft gels

To solve (9) requires knowledge of the rheology of the viscoelastic solid, *i.e.*  $\lambda(s)$  and  $\mu(s)$ .<sup>49</sup> The simplest models of viscoelasticity are the Maxwell model and the Kelvin–Voigt model. The former is more applicable to fluids while the latter is typically applied to solids. However, these single spring-dashpot model do not capture the wide ranging viscoelastic behavior of complex solids. Many soft solids consist of cross-linked polymers and are typically known as power law gels where  $\mu'(s)$  and  $\mu''(s)$  both scale with time as  $t^{-n}$ .<sup>44,45</sup> Here,  $n$  is the power law exponent and its value typically ranges

from 0.5–1 based on the stoichiometry of the polymer mixture. For these materials, the complex modulus is given by

$$\tilde{\mu}(s) = \mu_0(1 + (i\omega t_v)^n) \quad (10)$$

Here,  $\mu_0$  is the static or reference shear modulus and  $t_v$  is a viscoelastic timescale. Note  $i\omega$  is the complex frequency which is the same as the unstable growth rate, *i.e.*,  $s = i\omega$ . Also,  $t_v = 0$  corresponds to the purely elastic limit. The  $n = 1$  case corresponds to the Kelvin–Voigt limit, in which the term  $\mu_0 t_v$  becomes the solid viscosity. For this reason (10) is sometimes referred to as the fractional Kelvin–Voigt model.<sup>50</sup> Other fractional models have been put forth<sup>51</sup> and it would be straightforward to analyze these cases by simply substituting the functional form of  $\tilde{\mu}$  in (9).

## 3 Solution

We construct a solution to (9) by introducing the potential functions ( $\Phi, \mathbf{F}$ ) and using the Helmholtz decomposition of the displacement field,

$$\mathbf{u} = \nabla\Phi + \nabla \times \mathbf{F}. \quad (11)$$

Here  $\Phi$  is a scalar potential and  $\mathbf{F}$  is a vector potential. Applying (11) to (9) results in a set of decoupled Helmholtz equations,

$$\nabla^2 \Phi - \alpha^2 \Phi = 0 \quad (12a)$$

$$\nabla^2 \mathbf{F} - \beta^2 \mathbf{F} = 0. \quad (12b)$$

Here,  $\alpha = s\sqrt{\frac{\rho}{\tilde{\lambda} + 2\tilde{\mu}}}$  and  $\beta = s\sqrt{\frac{\rho}{\tilde{\mu}}}$ . The general solution of (12) is given by

$$\Phi(r, z) = A_0 I_0 \left( r\sqrt{\alpha^2 + k_z^2} \right) e^{ik_z z} + B_0 K_0 \left( r\sqrt{\alpha^2 + k_z^2} \right) e^{ik_z z}, \quad (13a)$$

$$F_r(r, z) = A_r I_1 \left( r\sqrt{\beta^2 + k_z^2} \right) e^{ik_z z} + B_r K_1 \left( r\sqrt{\beta^2 + k_z^2} \right) e^{ik_z z}, \quad (13b)$$

$$F_\theta(r, z) = A_\theta I_1 \left( r\sqrt{\beta^2 + k_z^2} \right) e^{ik_z z} + B_\theta K_1 \left( r\sqrt{\beta^2 + k_z^2} \right) e^{ik_z z}, \quad (13c)$$

$$F_z(r, z) = A_z I_0 \left( r\sqrt{\beta^2 + k_z^2} \right) e^{ik_z z} + B_z K_0 \left( r\sqrt{\beta^2 + k_z^2} \right) e^{ik_z z}, \quad (13d)$$

where we have assumed axisymmetry, *i.e.* no  $\theta$  dependence, consistent with the Steiner symmetrization procedure which gives the most destabilizing disturbance.<sup>52,53</sup> Here,  $F_r, F_\theta, F_z$  are the scalar components of  $\mathbf{F}$ ,  $k_z$  is the wavenumber in the  $z$ -direction, and  $I$  and  $K$  are the modified Bessel functions of the first and second kind, respectively. The Bessel function  $I$  diverges at  $r \rightarrow \infty$ , while  $K$  diverges at  $r \rightarrow 0$ . Therefore, for the case of the cylinder we set  $B_0 = B_r = B_\theta = B_z = 0$  and for cylindrical cavity we set  $A_0 = A_r = A_\theta = A_z = 0$  to ensure a physical solution.

### 3.1 Nondimensionalization

We scale the lengths with undisturbed radius  $R$  and time with the capillary time scale  $\sqrt{\rho R^3/\sigma}$ . This gives rise to the following non-dimensional parameters,

$$k = k_z R, \quad \xi = s \sqrt{\frac{\rho R^3}{\sigma}}, \quad \Sigma = \frac{\sigma}{\mu_0 R}, \quad \tau = t_v \sqrt{\frac{\sigma}{\rho R^3}}, \quad \kappa = \sqrt{\frac{1-2\nu}{2(1-\nu)}},$$

$$\gamma_1 = \sqrt{\kappa^2 \xi^2 \tilde{\Sigma} + k^2}, \quad \gamma_2 = \sqrt{\xi^2 \tilde{\Sigma} + k^2}, \quad \tilde{\Sigma} = \frac{\Sigma_0}{1 + (\tau \xi)^n}.$$
(14)

Here,  $\xi$  is the non-dimensional growth rate and  $k$  the scaled wavenumber. Three dimensionless numbers appear;  $\kappa$  is a compressibility number that ranges from  $\kappa = 0$  for an incompressible  $\nu = 0.5$  material to  $\kappa = 1/\sqrt{2}$  for a fully compressible  $\nu = 0$  material,  $\tau$  is the solid Deborah number<sup>54</sup> that is a measure of the relaxation time of the material relative to the capillary time scale with  $\tau = 0$  corresponding to the purely elastic limit, and  $\Sigma$  is the elastocapillary number representing the relative balance of capillary and elastic forces. Experiments using agarose gels have obtained softness up to  $\Sigma \sim O(10)$ ,<sup>9,13</sup> while thin columns of ultrasoft gels can have even higher  $\Sigma$ .

### 3.2 Dispersion equations

Applying the solution (13) to the boundary conditions (4) and (5) yields a set of linear equations for the unknown  $A$ 's in the cylinder case and the unknown  $B$ 's for the cylindrical cavity. The solvability condition for each case gives the corresponding dispersion relationship.

**3.2.1 Solid cylinder.** We begin with the case of the cylinder and write the boundary conditions (4) and (5) as

$$A_0 \left( \frac{\gamma_2^2 + k^2}{2} I_0(\gamma_1) - \gamma_1 I_1(\gamma_1) \right) - A_\theta ik (\gamma_2 I_0(\gamma_2) - I_1(\gamma_2))$$

$$= A_0 \frac{\tilde{\Sigma}}{2} (1 - k^2) \gamma_1 I_1(\gamma_1) + A_\theta \frac{\tilde{\Sigma}}{2} ik (1 - k^2) I_1(\gamma_2),$$
(15a)

$$A_0 2ik \gamma_1 I_1(\gamma_1) + A_\theta (\gamma_2^2 + k^2) I_1(\gamma_2) = 0, \quad (15b)$$

$$A_r(ik)(\gamma_2 I_0(\gamma_2) - 2I_1(\gamma_2)) - A_\theta (\gamma_2^2 I_0(\gamma_2) - 2\gamma_2 I_1(\gamma_2)) = 0, \quad (15c)$$

$$A_r k I_1(\gamma_2) + A_\theta i \gamma_2 I_1(\gamma_2) = 0. \quad (15d)$$

Note that (15a) and (15b) and (15c) and (15d) are decoupled and admit two classes of solution. Our focus is on the shape change modes which are described by eqn (15a) and (15b), whose solvability condition generates the dispersion relationship

$$2k^2 \gamma_1 \gamma_2 I_0(\gamma_2) I_1(\gamma_1) - \frac{1}{2} (\gamma_2^2 + k^2)^2 I_0(\gamma_1) I_1(\gamma_2)$$

$$+ \left( 1 + \frac{\tilde{\Sigma}}{2} (1 - k^2) \right) \gamma_1 (\gamma_2^2 - k^2) I_1(\gamma_1) I_1(\gamma_2) = 0. \quad (16)$$

**3.2.2 Cylindrical cavity.** Similarly, we can write the boundary conditions (4) and (5) for the cylindrical cavity as

$$B_0 \left( \frac{\gamma_2^2 + k^2}{2} K_0(\gamma_1) + \gamma_1 K_1(\gamma_1) \right) + B_\theta ik (\gamma_2 B_0(\gamma_2) + K_1(\gamma_2))$$

$$= B_0 \frac{\tilde{\Sigma}}{2} (1 - k^2) \gamma_1 K_1(\gamma_1) + B_\theta \frac{\tilde{\Sigma}}{2} ik (1 - k^2) K_1(\gamma_2),$$
(17a)

$$B_0 2ik \gamma_1 K_1(\gamma_1) - B_\theta (\gamma_2^2 + k^2) K_1(\gamma_2) = 0, \quad (17b)$$

$$B_r(ik) I_0(\gamma_2) + B_z \gamma_2 I_0(\gamma_2) = 0, \quad (17c)$$

$$B_r k I_1(\gamma_2) - B_z i \gamma_2 I_1(\gamma_2) = 0. \quad (17d)$$

The solvability condition for the shape modes (17a) and (17b) gives the dispersion relationship

$$2k^2 \gamma_1 \gamma_2 K_0(\gamma_2) K_1(\gamma_1) - \frac{1}{2} (\gamma_2^2 + k^2)^2 K_0(\gamma_1) K_1(\gamma_2)$$

$$- \left( 1 - \frac{\tilde{\Sigma}}{2} (1 - k^2) \right) \gamma_1 (\gamma_2^2 - k^2) K_1(\gamma_1) K_1(\gamma_2) = 0 \quad (18)$$

## 4 Results

The dispersion curve  $\xi(k)$  can be computed numerically from (16) and (18) for the rod and cylindrical cavity, respectively. For reference, the dispersion relationship for the classical PRI is given by,<sup>11</sup>

$$\xi^2 = (1 - k^2) k \frac{I_1(k)}{I_0(k)}, \quad (19)$$

which neglects both viscosity and elasticity. In what follows, we systematically investigate how the dispersion relationship depends upon the dimensionless numbers  $\Sigma$ ,  $\kappa$ ,  $\tau$ ,  $n$  focusing on the role of viscoelasticity. We start with the rod and begin by focusing on the purely elastic limit  $\tau = 0$  before showing how viscoelasticity affects stability. We then analyze the cylindrical cavity highlighting the difference with the cylindrical rod.

### 4.1 Solid cylinder

Fig. 2 plots the dispersion curves, growth rate  $\xi$  against wavenumber  $k$ , for a purely elastic  $\tau = 0$  material illustrating the competing roles of elastocapillarity  $\Sigma$  and compressibility  $\kappa$ . Most soft gels are hydrogels that are comprised mainly of water such that they are incompressible  $\kappa = 0$ .<sup>39,55</sup> Fig. 2(a) plots the dispersion curve for an incompressible material  $\kappa = 0$  for a range of elastocapillary numbers  $\Sigma$ . Each curve exhibits a range of unstable wavenumbers  $k_s$  that define the static limit  $\xi = 0$  and a maximum growth rate  $\xi_m$  that occurs at a wavenumber  $k_m$ . In the limit  $\Sigma \rightarrow \infty$ , we recover the PRI as could be expected. Increasing the elasticity relative to surface tension corresponds to decreasing the elastocapillary number  $\Sigma$ , which is shown to be stabilizing in that both the maximum growth rate  $\xi_m$  and range of unstable wavenumbers  $k_s$  shrink. In contrast, increasing the compressibility  $\kappa$  is destabilizing, as shown in Fig. 2(b). Note that

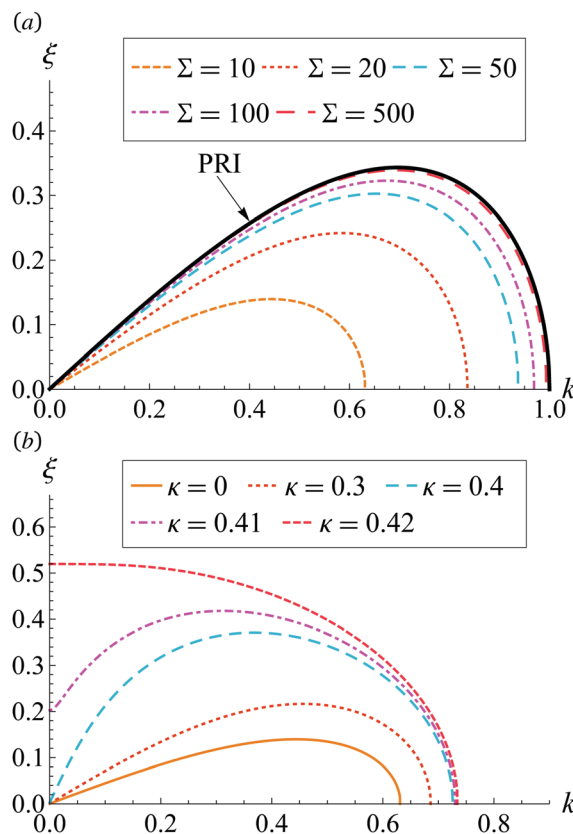


Fig. 2 Dispersion curves for a cylinder plotting growth rate  $\xi$  against wavenumber  $k$  for a purely elastic solid  $\tau = 0$ , as it depends upon (a) the elastocapillary number  $\Sigma$  for an incompressible  $\kappa = 0$  material and (b) compressibility number  $\kappa$  for fixed  $\Sigma = 10$ . The solid line is the dispersion relation for the PRI, eqn (19).

the wavenumber of maximum growth  $k_m$  shifts to a long wavelength  $k_m = 0$  disturbance for a range of  $\kappa$ , which corresponds to a uniform shrinking or collapse of the cylinder due to capillarity.

The relative balance between stabilizing elasticity and destabilizing compressibility gives rise to the stability diagram shown in Fig. 3 plotted in the  $\Sigma - \kappa$  parameter space for a purely elastic material  $\tau = 0$ . Here the incompressible  $\kappa = 0$  limit agrees with the static analysis of Mora *et al.*<sup>13</sup> which yields the threshold value  $\Sigma = 6$ . As the compressibility  $\kappa$  increases, the threshold value of elastocapillary number  $\Sigma$  decreases to  $\Sigma = 2$  at  $\kappa = 1/\sqrt{2}$ . Notably, this limit has been reported as the instability threshold for the cylindrical cavity by Xuan *et al.*,<sup>27</sup> which we discuss further shortly.

Although most gels used in experiment can be reasonably approximated to be incompressible materials, compressible gels might be useful to specific applications.<sup>56</sup> Compressibility can destabilize beyond the PRI limit. Fig. 4 shows how the stability properties  $k_s$ ,  $k_m$ ,  $\xi_m$  are affected by the compressibility  $\kappa$  for a purely elastic  $\tau = 0$  cylinder. The stability limit  $k_s$  is a monotonically increasing function  $\kappa$ , whereas the properties of the critical disturbance are more complex. The maximum

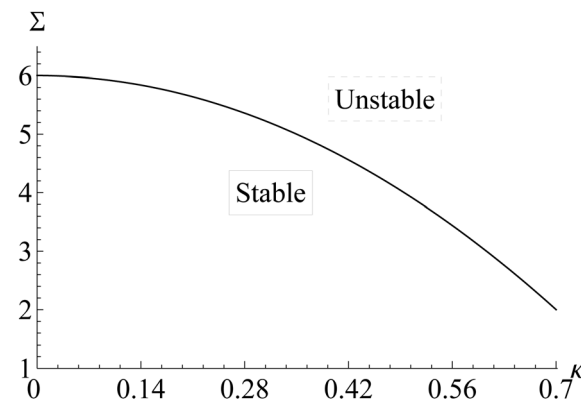


Fig. 3 Stability diagram for the purely elastic  $\tau = 0$  cylinder in the parameter space defined by the elastocapillary  $\Sigma$  and compressibility  $\kappa$  numbers.

growth rate  $\xi_m$  similarly increases monotonically with both  $\Sigma$  and  $\kappa$ , but the critical wavenumber displays a more complex dependence on  $\Sigma$ ,  $\kappa$ . For large elastocapillary number  $\Sigma = 20$ ,  $k_m$  monotonically decreases with  $\kappa$  until the long wavelength  $k = 0$  limit is reached, whereas for small elastocapillary number  $\Sigma = 7$ ,  $k_m$  increases with  $\kappa$ , reaches a maximum value and then rapidly decreases to  $k = 0$ . This highlights a complex interplay between surface tension, elasticity, and compressibility.

**4.1.1 Viscoelasticity.** Eqn (19) is the PRI dispersion relationship for an inviscid liquid cylinder, which exhibits three main properties; (1) the most unstable wavenumber is  $k_m = 0.697$ , (2) the growth rate for the most unstable wavenumber is  $\xi_m = 0.343$ , and (3) the static stability limit is  $k_s = 1$ . This result is an upper bound for an incompressible elastic solid  $\kappa = 0$ , as elasticity is shown to be a stabilizing effect (*cf.* Fig. 2(a)).

Viscoelasticity is also stabilizing and is described in our model by the Deborah number  $\tau$  and exponent  $n$ . Fig. 5 plots the dispersion relationship  $\xi$  against  $k$ , as it depends upon these viscoelastic properties. In Fig. 5(a), we show that the growth rate  $\xi$  decreases and  $k_m$  shifts to lower wavenumbers as  $\tau$  increases from the purely elastic limit  $\tau = 0$ . The effect of the exponent  $n$  is shown in Fig. 5(b) with increased damping associated with decreasing  $n$  with the Kelvin–Voigt case  $n = 1$  being the most unstable in this range of parameters. Note that the static stability limit  $k_s$  is unaffected by both  $\tau$  and  $n$  (*cf.* Fig. 5). That is, viscoelasticity damps the growth rate but does not change the range of unstable wavenumbers. This is further illustrated in Fig. 6(a) which plots  $k_s$  against the elastocapillary number  $\Sigma$  showing that  $\tau$  has no effect on the stability limit. However,  $\tau$  does shift  $k_m$  to lower wavenumbers and decreases  $\xi_m$ , as shown in Fig. 6(b and c), respectively. Again, the  $\Sigma \rightarrow \infty$  is the most unstable situation, regardless of  $\tau$  and  $n$ .

The critical disturbance  $k_m$  and associated growth rate  $\xi_m$  are shown in Fig. 7, as they depend upon the elastocapillary number  $\Sigma$  and solid Deborah number  $\tau$ . The trend is monotonic in both dimensionless numbers; the growth rate increases with (i) increasing  $\Sigma$  and (ii) decreasing  $\tau$ . The same monotonic trends exist for variations in the exponent  $n$ .

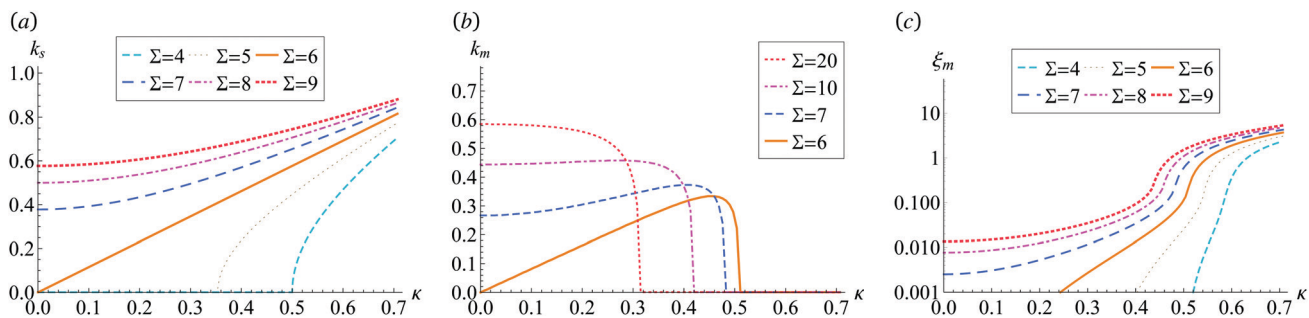


Fig. 4 Stability characteristics for a compressible purely elastic  $\tau = 0$  cylinder plotting (a) the static stability limit  $k_s$ , (b) critical wavenumber  $k_m$ , and (c) maximum growth rate  $\xi_m$  against the compressibility  $\kappa$ , as it depends upon the elastocapillary number  $\Sigma$ .

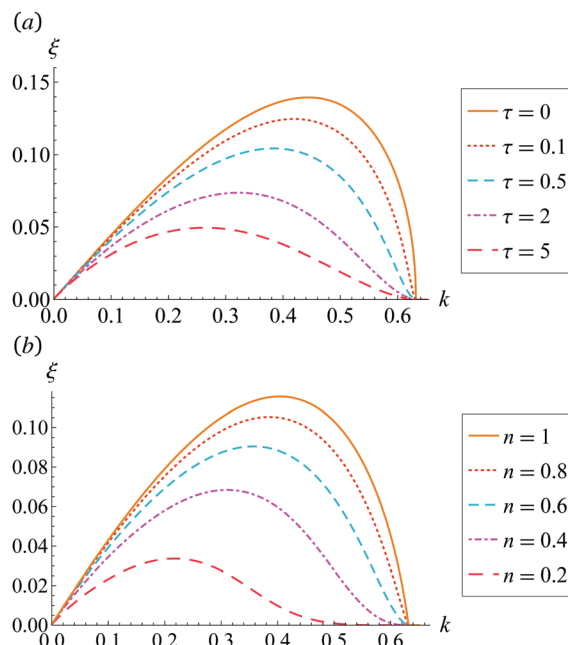


Fig. 5 Viscoelastic effects illustrated in the dispersion relationship plotting growth rate  $\xi$  against wavenumber  $k$ , as it depends upon (a) solid Deborah number  $\tau$  ( $\Sigma = 10$ ,  $n = 0.5$ ) and (b) exponent  $n$  ( $\Sigma = 10$ ,  $\tau = 1$ ).

#### 4.2 Cylindrical cavity

Fig. 8 plots the growth rate  $\xi$  against wavenumber  $k$  for a cylindrical cavity immersed in a purely elastic  $\tau = 0$  material. For an

incompressible material  $\kappa = 0$ , decreasing  $\Sigma$ , *i.e.* increasing elasticity, is stabilizing (*cf.* Fig. 8(a)). In the capillary limit  $\Sigma \rightarrow \infty$ , the dispersion approaches the PRI limit for a cylindrical cavity,

$$\xi^2 = (1 - k^2) \frac{K_1(k)}{K_0(k)}, \quad (20)$$

which admits the stability characteristics,  $k_s = 1$ ,  $k_m = 0.484$ ,  $\xi_m = 0.82$ . For an incompressible material  $\kappa = 0$ , this is the most unstable situation. In contrast, for fixed  $\Sigma$  increasing the compressibility of the material is destabilizing (*cf.* Fig. 8(b)). Interestingly, the static stability limit  $k_s$  is nearly unaffected by  $\kappa$  unlike the case of the cylinder (*cf.* Fig. 2(b)). The stability boundary is given by  $\Sigma = 2$  irrespective of  $\kappa$  and this agrees with previous literature.<sup>27</sup>

Fig. 9 plots the stability characteristics ( $k_s$ ,  $k_m$ ,  $\xi_m$ ) for a purely elastic  $\tau = 0$  cylindrical cavity against the compressibility  $\kappa$ . The static stability limit  $k_s$  shows a very weak dependence upon  $\kappa$  that increases with  $\Sigma$  (*cf.* Fig. 9(a)). The critical wavenumber  $k_m$  decreases with increasing compressibility  $\kappa$  and eventually becomes  $k_m = 0$  at a critical value of the compressibility  $\kappa^*$  which decreases with increasing  $\Sigma$  (*cf.* Fig. 9(b)). The maximum growth rate  $\xi_m$  increases with both  $\Sigma$  and  $\kappa$ , as shown in Fig. 9(c). Lastly, we note that the growth rate remains the same order of magnitude over the entire range of  $\kappa$ , unlike the cylinder whose growth rate varied substantially with  $\kappa$  (*cf.* Fig. 4(c)).

**4.2.1 Viscoelasticity.** Similar to the cylinder, viscoelasticity affects the critical wavenumber  $k_m$  and growth rate  $\xi_m$ , but not the static stability limit  $k_s$  for the incompressible  $\kappa = 0$

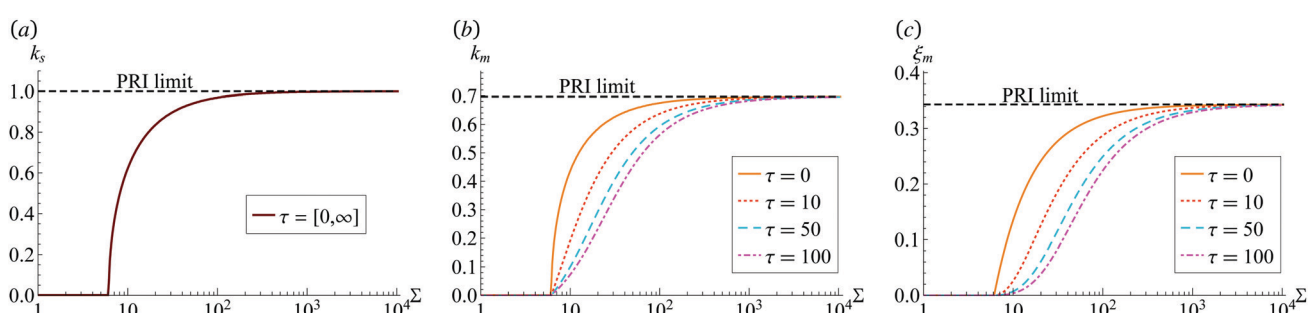


Fig. 6 Stability characteristics of an incompressible  $\kappa = 0$  viscoelastic cylinder plotting the (a) static stability limit  $k_s$ , (b) critical wavenumber, and (c) maximum growth rate  $\xi_m$  against the elastocapillary number  $\Sigma$ , as it depends upon the solid Deborah number  $\tau$  for  $n = 0.5$ . The dashed line denotes the PRI limit.

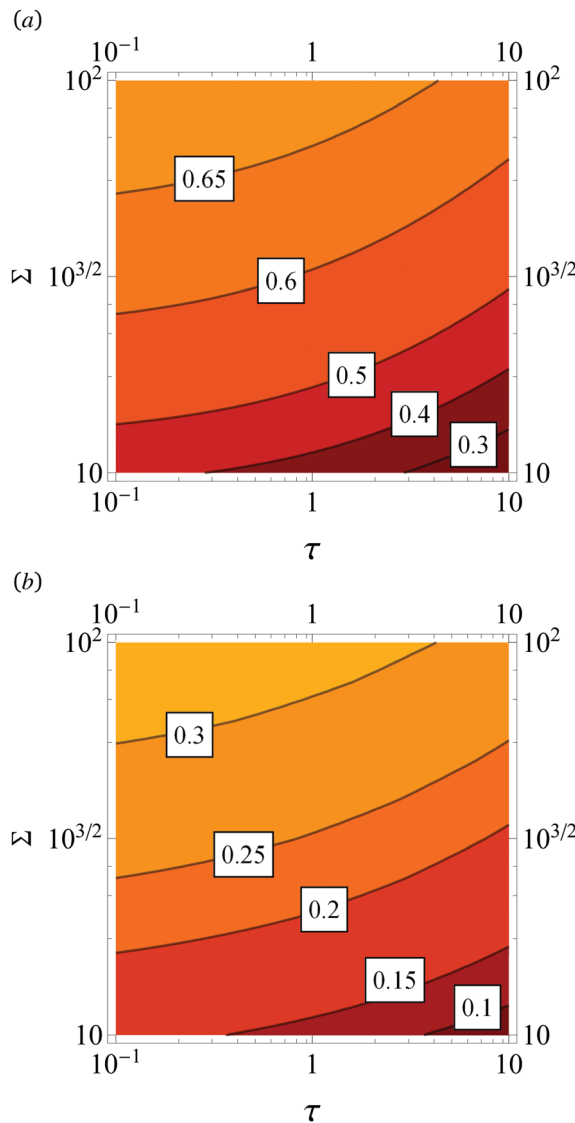


Fig. 7 Critical disturbance plotting (a) the wavenumber  $k_m$  and (b) growth rate  $\xi_m$  against the elastocapillary number  $\Sigma$  and solid Deborah number  $\tau$  for an incompressible  $\kappa = 0$  cylinder with  $n = 0.5$ .

cylindrical cavity, as shown in Fig. 10. Increasing the solid Deborah number  $\tau$  shifts  $k_m$  to lower wavenumbers and decreases the growth rate for fixed  $\Sigma$ . In the limit  $\Sigma \rightarrow \infty$ , the PRI limit is approached and the effect of  $\tau$  is negligible.

Fig. 11 plots the critical disturbance  $k_m$  and associated growth rate  $\xi_m$  for the incompressible  $\kappa = 0$  cylindrical cavity, as they depend upon the elastocapillary number  $\Sigma$  and solid Deborah number  $\tau$ . The trend is monotonic in both dimensionless numbers; the growth rate increases with (i) increasing  $\Sigma$  and (ii) decreasing  $\tau$ .

## 5 Comparison with experiment

Here we compare our results to the experimental data on capillary driven instability in solid cylinders by Mora *et al.*<sup>13</sup>

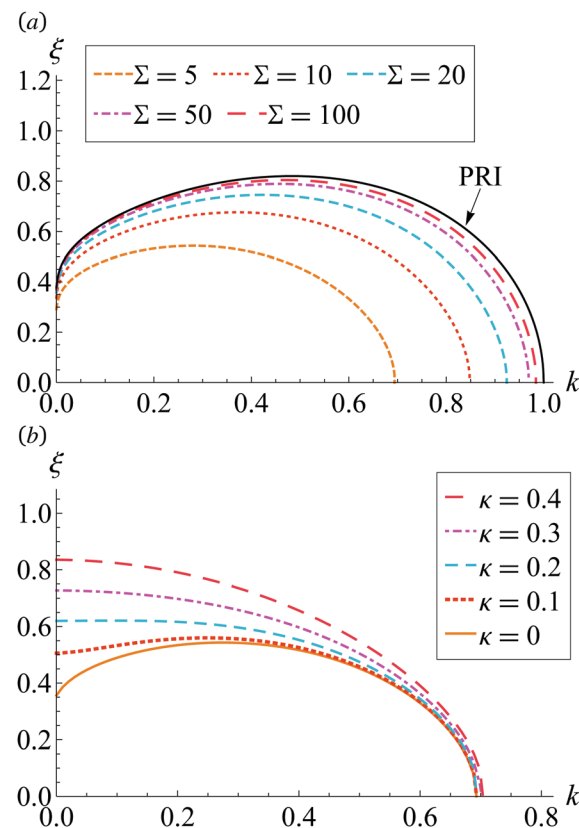


Fig. 8 Dispersion curves for a cylindrical cavity plotting growth rate  $\xi$  against wavenumber  $k$ , as it depends upon (a) the elastocapillary number  $\Sigma$  for  $\kappa = 0$  and (b) compressibility number  $\kappa$  for  $\Sigma = 5$ . The solid line is the PRI dispersion for a cylindrical cavity given by eqn (20).

Their experiments were performed using thin cylinders ( $R = 240 \mu\text{m}$ ) of agar and show the emergence of an unstable wavy undulation along the axis of the cylinder. The instability disappeared with decreasing elastocapillary number  $\Sigma < 6$ , consistent with predictions from our model. For a cylinder with  $\Sigma = 10.6$  (Mora *et al.* Fig. 2d), they observed an unstable wavelength  $\lambda \approx 30R$ , which is much longer than that predicted by Rayleigh's theory  $\lambda \approx 9.1R$ . This is presumably due to the elasticity of the agar gel. Our purely elastic solution ( $\tau = 0$ ) predicts wavelengths  $\lambda \approx 13R$ , longer than the Rayleigh limit, but still lower than experimental observation. We hypothesize that this discrepancy is due to a viscoelastic effect which shifts to longer wavelengths according to our model (cf. Fig. 5). Even though the capillary time scale is small  $\approx 10^{-3}$  s, the non-dimensional viscoelastic relaxation time  $\tau$  can be  $O(1)$  for materials with short relaxation times, as is true for the agar gels used in the experiments by Mora *et al.* Fig. 1. As shown in Fig. 5, increasing  $\tau$  leads to smaller  $k_m$ , *i.e.*, longer critical wavelengths. Also, the Ohnesorge number  $\left( \text{Oh} = \frac{G_0 t_v}{\sqrt{\rho \sigma R}} \right)$  corresponding to the parameters in the Mora experiment should be larger than 1. This shows the importance of including solid viscoelasticity in the dynamic stability analysis. If we assume a simple Kelvin–Voigt rheology ( $n = 1$ ) we can fit the observed wavelength from experiment for  $\Sigma = 10.6$  to our model when

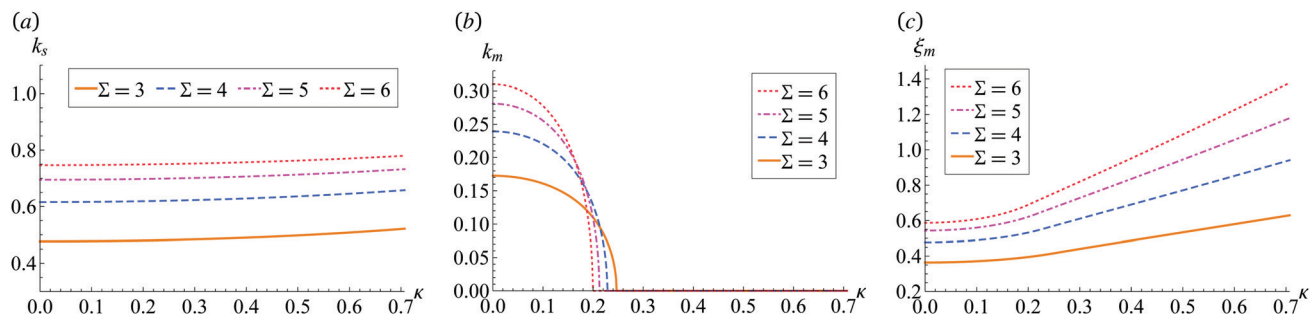


Fig. 9 Stability characteristics for a compressible purely elastic  $\tau = 0$  cylindrical cavity plotting (a) the static stability limit  $k_s$ , (b) critical wavenumber  $k_m$ , and (c) maximum growth rate  $\xi_m$  against the compressibility  $\kappa$ , as it depends upon the elastocapillary number  $\Sigma$ .

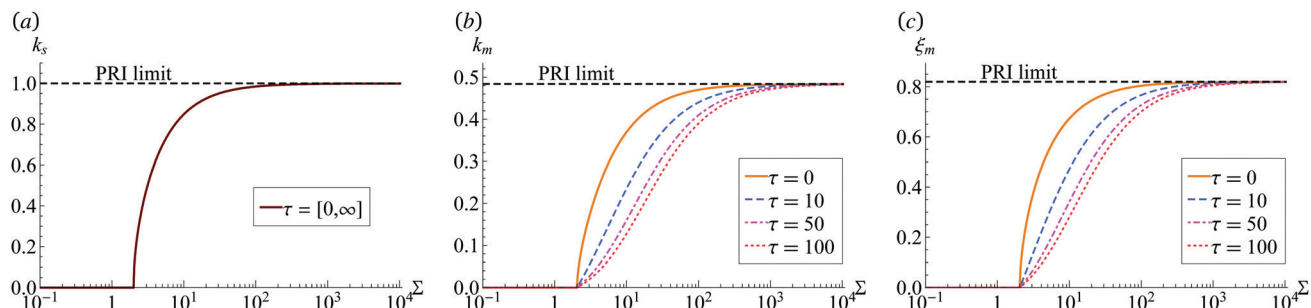


Fig. 10 Stability characteristics for an incompressible  $\kappa = 0$  cylindrical cavity plotting (a) the static stability limit  $k_s$ , (b) critical wavenumber  $k_m$ , and (c) maximum growth rate  $\xi_m$  against the elastocapillary number  $\Sigma$ , as it depends upon the solid Deborah number  $\tau$  for  $n = 1$ . Dashed line refer to the PRI limit.

$\tau = 5$ . This shows the importance of including viscoelastic effects into the analysis to predict critical wavelength. Furthermore, a recent paper has also shown through numerical nonlinear analysis that the final modes are indeed selected by a dynamic process.<sup>23</sup>

## 6 Concluding remarks

We have developed a model for the PRI in viscoelastic solids for the complementary geometries of the cylinder and cylindrical cavity. Dispersion relationships have been derived and depend upon the non-dimensional numbers  $\Sigma$ ,  $\tau$ ,  $\kappa$ , which account for elastocapillary, viscoelasticity, and compressibility, respectively. Our dynamic model is distinguished in that we predict the critical wavenumber  $k_m$  of maximum growth rate  $\xi_m$  that should be observed in experiment, and we also recover the previously reported static stability results for the incompressible cylinder  $\Sigma = 6$ <sup>13</sup> and incompressible cylindrical cavity  $\Sigma = 2$ <sup>27</sup> by setting the growth rate  $\xi = 0$ . This approach is similar to how Rayleigh's dynamic analysis<sup>11</sup> complemented the static analysis of Plateau<sup>10</sup> for the PRI. Both elasticity and viscoelasticity are stabilizing effects, whereas compressibility is destabilizing. For an incompressible material, viscoelasticity does not affect the range of unstable wavenumbers  $k_s$ , but does affect the critical disturbance by shifting  $k_m$  to lower wavenumbers and decreasing the growth rate  $\xi_m$  (cf. Fig. 6 and 10). The effect of the power law exponent  $n$  is quantitative but does not qualitatively change our

results. For a compressible material, the stability limit for  $\Sigma$  decreases with increasing  $\kappa$  for the cylinder, but is a constant  $\Sigma = 2$  for the cylindrical cavity and independent of compressibility. For the cylinder, compressibility increases the range of unstable wavenumbers  $k_s$  and increases the growth rate  $\xi_m$ , but the critical wavenumber  $k_m$  has a more complex dependence on  $\Sigma$ ,  $\kappa$ , as shown in Fig. 4. The associated trends for the cylindrical cavity are more monotonic (cf. Fig. 9).

The classic PRI of an inviscid liquid sees the cylindrical jet breakup into spherical droplets in what are naturally large-amplitude disturbances. Soft solids tend to show nonlinear behavior at large strain<sup>57</sup> and this causes the PRI to assume an undulating shape in experiment.<sup>13</sup> Our analysis assumes small strains, but still should be able to describe the instability mechanism, predict the stability limit, as well as the critical disturbance which often persists (*i.e.* the linear mode quenches itself) in weakly nonlinear analysis provided the bifurcation is supercritical.<sup>58</sup> Nevertheless, understanding the role of nonlinear elasticity and complex rheology of soft solids has seen sustained interest among researchers.<sup>61</sup> Yield stress materials behave elastically beyond the jamming transition threshold. This enhances the stability of 3D printed structures<sup>59</sup> pointing to a nonlinear response of the material. Future directions in the study of the PRI could focus on large strains in the nonlinear regime and how this affects the morphology of the instability. This will aid in developing fabrication techniques for soft solids, *i.e.* bioprinting, which exploit pattern formation, as these are naturally large amplitude disturbances. Lastly, the techniques

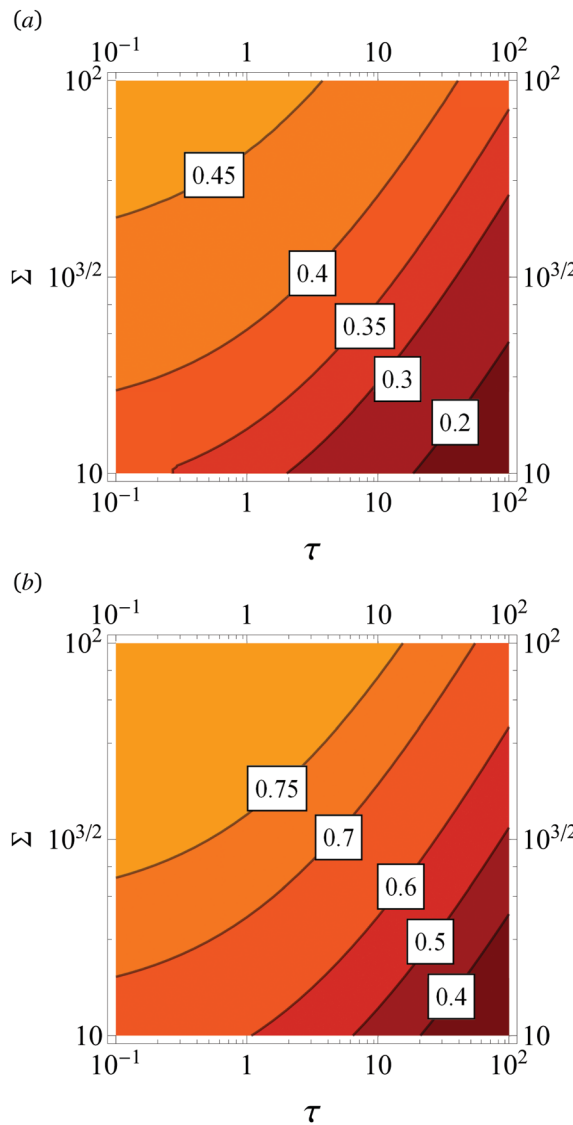


**Fig. 11** Critical disturbance plotting (a) the wavenumber  $k_m$  and (b) growth rate  $\xi_m$  against the elastocapillary number  $\Sigma$  and solid Deborah number  $\tau$  for an incompressible  $\kappa = 0$  cylindrical cavity with  $n = 0.6$ .

developed here could be used to model other systems, *e.g.*, soft tubes or channels of finite thickness filled with a flowing viscous fluid, that could shed light on other dynamic elastocapillary phenomena.

## Conflicts of interest

There are no conflicts to declare.

## Appendix: cylindrical components

The displacement and stress components required for derivation of the dispersion relations are obtained using general solutions in eqn (13).

### A.1 Cylinder

The displacement components of a solid cylinder are,

$$u_r = (A_0 a I_1(ar) - A_\theta (ik_z) I_1(br)) e^{ik_z z}, \quad (21a)$$

$$u_\theta = (A_r (ik_z) I_1(br) - A_z b I_1(br)) e^{ik_z z}, \quad (21b)$$

$$u_z = (A_0 (ik_z) I_0(ar) + A_\theta b I_0(br)) e^{ik_z z}, \quad (21c)$$

where  $a = \sqrt{\alpha^2 + k_z^2}$ ,  $b = \sqrt{\beta^2 + k_z^2}$ . Using the constitutive relation (7), the stresses are obtained as

$$\begin{aligned} \tau_{rr} = 2\tilde{\mu} & \left[ A_0 \left( \frac{b^2 + k_z^2}{2} I_0(ar) - \frac{a}{r} I_1(ar) \right) \right. \\ & \left. - A_\theta (ik_z) \left( b I_0(br) - \frac{1}{r} I_1(br) \right) \right] e^{ik_z z}, \end{aligned} \quad (22a)$$

$$\tau_{rz} = \tilde{\mu} [A_0 (ik_z) 2a I_1(ar) + A_\theta (b^2 + k_z^2) I_1(br)] e^{ik_z z}, \quad (22b)$$

$$\begin{aligned} \tau_{r\theta} = \tilde{\mu} & \left[ A_r (ik_z) \left( b I_0(br) - \frac{2}{r} I_1(br) \right) \right. \\ & \left. - A_z \left( b^2 I_0(br) - \frac{2b}{r} I_1(br) \right) \right] e^{ik_z z}, \end{aligned} \quad (22c)$$

$$\tau_{\theta z} = \tilde{\mu} [-A_r k_z^2 I_1(br) - A_z b (ik_z) I_1(br)] e^{ik_z z}. \quad (22d)$$

### A.2 Cylindrical cavity

Similarly for a hollow cylindrical cavity, the displacement components are

$$u_r = (-B_0 a K_1(ar) - B_\theta (ik_z) K_1(br)) e^{ik_z z}, \quad (23a)$$

$$u_\theta = (B_r (ik_z) K_1(br) + B_z b K_1(br)) e^{ik_z z}, \quad (23b)$$

$$u_z = (B_0 (ik_z) K_0(ar) - B_\theta b K_0(br)) e^{ik_z z}, \quad (23c)$$

and the stress components are

$$\begin{aligned} \tau_{rr} = 2\tilde{\mu} & \left[ B_0 \left( \frac{b^2 + k_z^2}{2} K_0(ar) + \frac{a}{r} K_1(ar) \right) \right. \\ & \left. + B_\theta (ik_z) \left( b K_0(br) + \frac{1}{r} K_1(br) \right) \right] e^{ik_z z}, \end{aligned} \quad (24a)$$

$$\tau_{rz} = \tilde{\mu} [-B_0 (ik_z) 2a K_1(ar) + B_\theta (b^2 + k_z^2) K_1(br)] e^{ik_z z}, \quad (24b)$$

$$\tau_{r\theta} = \tilde{\mu} [B_r (ik_z) b K_0(br) + B_z b^2 K_0(br)] e^{ik_z z}, \quad (24c)$$

$$\tau_{\theta z} = \tilde{\mu} [-B_r k_z^2 I_1(br) - B_z b (ik_z) I_1(br)] e^{ik_z z}. \quad (24d)$$

## Notes and references

- 1 R. Shuttleworth, *Proc. Phys. Soc., London, Sect. A*, 1950, **63**, 444.

2 B. Andreotti, O. Bäumchen, F. Boulogne, K. E. Daniels, E. R. Dufresne, H. Perrin, T. Salez, J. H. Snoeijer and R. W. Style, *Soft Matter*, 2016, **12**, 2993–2996.

3 R. W. Style, A. Jagota, C.-Y. Hui and E. R. Dufresne, *Ann. Rev. Condens. Matter Phys.*, 2017, **8**, 99–118.

4 J. Bico, É. Reyssat and B. Roman, *Annu. Rev. Fluid Mech.*, 2018, **50**, 629–659.

5 S. Mora, T. Phou, J.-M. Fromental and Y. Pomeau, *Phys. Rev. Lett.*, 2014, **113**, 178301.

6 S. Tamim and J. Bostwick, *Soft Matter*, 2019, **15**, 9244–9252.

7 B. Saintyves, O. Dauchot and E. Bouchaud, *Phys. Rev. Lett.*, 2013, **111**, 047801.

8 X. Shao, J. Saylor and J. Bostwick, *Soft Matter*, 2018, **14**, 7347–7353.

9 X. Shao, S. Fredericks, J. Saylor and J. Bostwick, *Phys. Rev. Lett.*, 2019, **123**, 188002.

10 J. Plateau, *Statique expérimentale et théorique des liquides soumis aux seules forces moléculaires*, Gauthier-Villars, 1873, vol. 2.

11 L. Rayleigh, *Proc. Lond. Math. Soc.*, 1878, **1**, 4–13.

12 L. Rayleigh, *Philos. Mag. Ser.*, 1892, **34**, 177–180.

13 S. Mora, T. Phou, J.-M. Fromental, L. M. Pismen and Y. Pomeau, *Phys. Rev. Lett.*, 2010, **105**, 214301.

14 S. Ji and M. Guvendiren, *Front. Bioeng. Biotechnol.*, 2017, **5**, 23.

15 O. A. Basaran, H. Gao and P. P. Bhat, *Annu. Rev. Fluid Mech.*, 2013, **45**, 85–113.

16 R. Karyappa, T. Ching and M. Hashimoto, *ACS Appl. Mater. Interfaces*, 2020, **12**, 23565–23575.

17 L. Mecozzi, O. Gennari, S. Coppola, F. Olivieri, R. Rega, B. Mandracchia, V. Vespi, A. Bramanti, P. Ferraro and S. Grilli, *ACS Appl. Mater. Interfaces*, 2018, **10**, 2122–2129.

18 E. Hannezo, J. Prost and J.-F. Joanny, *Phys. Rev. Lett.*, 2012, **109**, 018101.

19 A. L. Hazel and M. Heil, *Proc. R. Soc. A*, 2005, **461**, 1847–1868.

20 P. Ciarletta and M. B. Amar, *Soft Matter*, 2012, **8**, 1760–1763.

21 M. Taffetani and P. Ciarletta, *Phys. Rev. E: Stat., Nonlinear, Soft Matter Phys.*, 2015, **91**, 032413.

22 M. Taffetani and P. Ciarletta, *J. Mech. Phys. Solids*, 2015, **81**, 91–120.

23 A. Pandey, M. Kansal, M. A. Herrada, J. Eggers and J. H. Snoeijer, arXiv preprint arXiv:2012.08092, 2020.

24 C. Xuan and J. Biggins, *Phys. Rev. E*, 2017, **95**, 053106.

25 A. Giudici and J. S. Biggins, *Phys. Rev. E*, 2020, **102**, 033007.

26 P. P. Bhat, S. Appathurai, M. T. Harris, M. Pasquali, G. H. McKinley and O. A. Basaran, *Nat. Phys.*, 2010, **6**, 625–631.

27 C. Xuan and J. Biggins, *Phys. Rev. E*, 2016, **94**, 023107.

28 N. Cheewaruangroj, K. Leonavicius, S. Srinivas and J. S. Biggins, *Phys. Rev. Lett.*, 2019, **122**, 068003.

29 L. Wang, *Int. J. Solids Struct.*, 2020, **191**, 341–350.

30 S. Middleman, *Chem. Eng. Sci.*, 1965, **20**, 1037–1040.

31 G. H. McKinley, *Annu. Rheol. Rev.*, 2005, 1–49.

32 D. T. Chen, Q. Wen, P. A. Janmey, J. C. Crocker and A. G. Yodh, *Annu. Rev. Condens. Matter Phys.*, 2010, **1**, 301–322.

33 X. Zhao, N. Huebsch, D. J. Mooney and Z. Suo, *J. Appl. Phys.*, 2010, **107**, 063509.

34 M. M. Fitzgerald, K. Bootsma, J. A. Berberich and J. L. Sparks, *Biomacromolecules*, 2015, **16**, 1497–1505.

35 T. Gao, G. J. Gillispie, J. S. Copus, A. K. Pr, Y.-J. Seol, A. Atala, J. J. Yoo and S. J. Lee, *Biofabrication*, 2018, **10**, 034106.

36 N. Reddy, R. Reddy and Q. Jiang, *Trends Biotechnol.*, 2015, **33**, 362–369.

37 Y. Zhang, S. T. Ellison, S. Duraivel, C. D. Morley, C. R. Taylor and T. E. Angelini, *Bioprinting*, 2021, **21**, e00121.

38 P. Zhu, W. Yang, R. Wang, S. Gao, B. Li and Q. Li, *ACS Appl. Mater. Interfaces*, 2018, **10**, 36435–36442.

39 M. Tokita and K. Hikichi, *Physical Review A*, 1987, **35**, 4329.

40 T. Kajiyama, A. Daerr, T. Narita, L. Royon, F. Lequeux and L. Limat, *Soft Matter*, 2013, **9**, 454–461.

41 S. Park, J. Bostwick, V. De Andrade and J. Je, *Soft Matter*, 2017, **13**, 8331–8336.

42 A. Wineman, *Math. Mech. Solids*, 2009, **14**, 300–366.

43 S. Karpitschka, S. Das, M. van Gorcum, H. Perrin, B. Andreotti and J. H. Snoeijer, *Nat. Commun.*, 2015, **6**, 1–7.

44 H. H. Winter and F. Chambon, *J. Rheol.*, 1986, **30**, 367–382.

45 F. Chambon and H. H. Winter, *J. Rheol.*, 1987, **31**, 683–697.

46 H. Kibbelaar, A. Deblais, F. Burla, G. Koenderink, K. Velikov and D. Bonn, *Phys. Rev. Fluids*, 2020, **5**, 092001.

47 J. Eggers, M. A. Herrada and J. Snoeijer, *J. Fluid Mech.*, 2020, **887**, A19.

48 R. Christensen, *Theory of viscoelasticity: an introduction*, Elsevier, 2012.

49 F. Mainardi and G. Spada, *Eur. Phys. J. Spec. Top.*, 2011, **193**, 133–160.

50 K. D. Papoulias, V. P. Panoskaltsis, N. V. Kurup and I. Korovajchuk, *Rheol. Acta*, 2010, **49**, 381–400.

51 A. Bonfanti, J. L. Kaplan, G. Charras and A. J. Kabla, *Soft Matter*, 2020, **16**, 6002–6020.

52 R. Gillette and D. Dyson, *Chem. Eng. J.*, 1972, **3**, 196–199.

53 J. Bostwick and P. Steen, *J. Fluid Mech.*, 2010, **647**, 201–219.

54 M. Reiner, *Phys. Today*, 1964, **17**, 62.

55 V. Normand, D. L. Lootens, E. Amici, K. P. Plucknett and P. Aymard, *Biomacromolecules*, 2000, **1**, 730–738.

56 A. Wahlsten, M. Pensalfini, A. Stracuzzi, G. Restivo, R. Hopf and E. Mazza, *Biomech. Model. Mechanobiol.*, 2019, **18**, 1079–1093.

57 C. Storm, J. J. Pastore, F. C. MacKintosh, T. C. Lubensky and P. A. Janmey, *Nature*, 2005, **435**, 191–194.

58 F. Charru and P. de Forcrand-Millard, *Hydrodynamic Instabilities*, Cambridge University Press, 2011.

59 C. S. O'Bryan, T. Bhattacharjee, S. L. Marshall, W. G. Sawyer and T. E. Angelini, *Bioprinting*, 2018, **11**, e00037.

60 S. Tamim and J. Bostwick, *Extreme Mech. Lett.*, 2020, **40**, 100940.

61 J. Snoeijer, A. Pandey, M. Herrada and J. Eggers, *Proc. R. Soc. A*, 2020, **476**, 20200419.

62 R. Suntornnond, J. An and C. K. Chua, *Macromol. Mater. Eng.*, 2017, **302**, 1600266.